The Astrophysical Journal, 987:31 (13pp), 2025 July 1 https://doi.org/10.3847/1538-4357/add6a8

Large-amplitude Whistler Precursors and >MeV Particles Observed at a Weak Interplanetary Shock by Parker Solar Probe

Lynn B. Wilson, III[1], J. Grant Mitchell[1], Adam Szabo[1], Immanuel C. Jebaraj[2], Michael L. Stevens[3], David M. Malaspina[4,5], Grant D. Berland[6], Athanasios Kouloumvakos[6], Stuart D. Bale[7,8], Roberto Livi[7,8], Jasper S. Halekas[9], and Christina M. S. Cohen[10]
[1] NASA Goddard Space Flight Center, Heliophysics Science Division, Greenbelt, MD, USA; lynn.b.wilsoniii@gmail.com
[2] University of Turku, Turku, Finland
[3] Harvard-Smithsonian Center for Astrophysics, Harvard University, Cambridge, MA, USA
[4] Astrophysical and Planetary Sciences department, University of Colorado Boulder, Boulder, CO, USA
[5] Laboratory for Atmospheric and Space Physics, University of Colorado Boulder, Boulder, CO, USA
[6] Johns Hopkins University Applied Physics Laboratory, Laurel, MD, USA
[7] Physics Department, University of California, Berkeley, CA 94720-7300, USA
[8] Space Sciences Laboratory, University of California, Berkeley, CA, USA
[9] University of Iowa, Iowa City, IA, USA
[10] California Institute of Technology, Pasadena, CA, USA
Received 2025 March 27; revised 2025 May 7; accepted 2025 May 7; published 2025 June 25

Abstract

We report observations of an interplanetary (IP) shock observed by Parker Solar Probe (PSP) on 2024 September 29 at ∼07:50:29 UTC. PSP was only ∼17.07 R_s from the Sun, making this one of the closest observed IP shocks to date. The IP shock was a weak ($M_f \sim 1.2$), quasi-perpendicular ($\theta_{Bn} \sim 50°$), and of moderate speed ($V_{shn} \sim 465$ km s^{-1}). The standard shock acceleration mechanisms (e.g., Fermi acceleration) predict that such an unremarkable shock cannot generate energetic particles (i.e., over 4 orders of magnitude above thermal energies), which is supported by decades of IP shock observations near 1 au. However, ∼MeV energy protons with an inverse velocity arrival and synchrotron radiation (due to ∼MeV energy electrons) were observed upstream. This raised the question of what was different about this shock. One observation was that of a fast/magnetosonic-whistler precursor with peak-to-peak magnetic field amplitudes >700 nT, electric fields >2000 mV m^{-1}, and Poynting fluxes >230 mW m^{-2}. These are 2 orders of magnitude larger than any previously observed whistler precursor. To put the amplitudes in context, the lower bound Poynting flux estimates are >200 times what is necessary to drive the terrestrial aurora. Note that the normalized wave parameters (e.g., frequency) were found to be consistent with previous studies near 1 au. Thus, the precursors cannot likely generate a larger fraction of energetic particles than similar precursors near 1 au. However, the much larger amplitudes would allow for higher maximum energies. This raises important questions about inaccessible shocks in more extreme astrophysical environments and what potential energization they may have in light of these observations.

Unified Astronomy Thesaurus concepts: Interplanetary shocks (829); Solar coronal mass ejection shocks (1997); Solar wind (1534); The Sun (1693)

1. Background and Motivation

Most collisionless shocks in astrophysical plasmas arise from a nonlinearly steepened fast/magnetosonic-whistler wave that reached a balance between steepening and some form of irreversible energy dissipation. If steepening is balanced by energy dissipation, a stationary discontinuity can initiate (R. Courant & K. O. Friedrichs 1977; F. H. Shu 1992). This discontinuity, known as the shock ramp, has a thickness that is predicted to depend upon macroscopic parameters like M_f (fast mode Mach number), θ_{Bn} (shock normal angle[11]), and upstream averaged plasma beta (R. Z. Sagdeev 1966; F. V. Coroniti 1970; D. A. Tidman & N. A. Krall 1971; A. A. Galeev 1976; C. F. Kennel et al. 1985) (see Appendix A for parameter definitions). Observations have shown that the ramp thickness of collisionless shocks varies from a few electron inertial lengths (λ_e) to an ion inertial length (λ_i), but most are below ∼35 λ_e (J. A. Newbury & C. T. Russell 1996; J. A. Newbury et al. 1998; Y. Hobara et al. 2010; C. Mazelle et al. 2010). The typical collisional mean free path of charged particles in the interplanetary (IP) medium near Earth is on the order of 1 au or $\gtrsim 10^7 \lambda_e$ (L. B. Wilson et al. 2018, 2023). Thus, these shocks are termed collisionless since the necessary energy dissipation cannot be derived from particle–particle collisions.

Electromagnetic fluctuations on the fast/magnetosonic-whistler dispersion relation branch are right-hand polarized in the plasma rest frame (PRF) with density oscillations in-phase with magnetic field magnitude oscillations. They are dispersive in such a way that the higher-frequency components have larger phase speeds. This led to early theories predicting wave trains upstream of the shock ramp (e.g., A. A. Galeev & V. I. Karpman 1963; V. I. Karpman 1964), called whistler precursors. For low Mach number, quasi-perpendicular shocks, these waves result from a process known as dispersive radiation (e.g., A. A. Galeev & V. I. Karpman 1963; T. E. Stringer 1963; K. W. Morton 1964; R. Z. Sagdeev 1966; D. A. Tidman & T. G. Northrop 1968; G. Decker & A. E. Robson 1972; M. M. Mellott & E. W. Greenstadt 1984; V. V. Krasnoselskikh

[11] For instance, quasi-perpendicular is defined as $\theta_{Bn} \geqslant 45°$.

et al. 2002). That is, the time- and spatially varying currents that cause the nonlinear steepening of the magnetic field radiate electromagnetic waves on the same branch of the dispersion relation. Since they are dispersive, the higher-frequency modes outrun the lower, and thus the wave train evolves. Whistler precursors have been observed upstream of low Mach number, quasi-perpendicular shocks for over 50 yr (e.g., D. H. Fairfield 1974; D. H. Fairfield & W. C. Feldman 1975; E. W. Greenstadt et al. 1975; M. M. Mellott & E. W. Greenstadt 1984; M. H. Farris et al. 1993; L. B. Wilson et al. 2009, 2017; P. Kajdič et al. 2012; J. C. Ramírez Vélez et al. 2012; D. Sundkvist et al. 2012; X. Blanco-Cano et al. 2016). They are consistently observed upstream of high Mach number, quasi-perpendicular shocks as well (e.g., M. A. Balikhin et al. 1999; S. N. Walker et al. 1999; A. J. Hull et al. 2012, 2020, 2024; L. B. Wilson et al. 2012, 2013, 2014a, 2014b), though they likely have a different generation mechanism than dispersive radiation. They are even observed upstream of quasi-parallel shocks (e.g., D. H. Fairfield & W. C. Feldman 1975; E. W. Greenstadt et al. 1977; E. W. Greenstadt 1985; C. T. Russell 1988; I. C. Jebaraj et al. 2024b). In fact, the waves are so consistently observed that L. B. Wilson et al. (2017) argued that shocks that do not appear to exhibit whistler precursors only because the instrument underresolves the fluctuations.

Whistler precursors are known to be important in the energy/momentum exchange between ions and electrons; thus, they are thought to play an important role in shock dissipation. They have been observed to locally energize electrons (e.g., L. B. Wilson et al. 2012), which led L. B. Wilson et al. (2016) to suggest they may play a critical role in the generation of relativistic electrons observed within foreshock transients. Recent simulations have shown that the combination of whistler precursors, higher-frequency whistler waves, high-frequency electrostatic waves, and the usual shock acceleration mechanisms (e.g., shock drift acceleration, Fermi acceleration, etc.) are all necessary to generate both the maximum energies and observed power-law slope (S. Raptis et al. 2025; X. Shi et al. 2025). The basic process is that the high-frequency electrostatic waves heat/scatter the thermal core, the precursors, and higher-frequency whistler waves stochastically scatter and accelerate the particles to higher energies, and once at sufficiently high energies, the efficiency of the usual shock acceleration mechanisms begins to greatly increase. Similar to IP shocks, the shocks generated by foreshock transients tend to be low Mach number and locally quasi-perpendicular; thus, similar mechanisms may be active.

This paper is outlined as follows: Section 2 describes the data sets and some of the methodologies used herein. Section 3 presents an overview of the shock analysis and macroscopic parameters. Section 4 presents the analysis of the whistler precursor, both minimum variance and wave amplitude analysis. Section 5 discusses the main results and some of the implications. And Section 6 summarizes the results and provides some context and thoughts on future work. We have also provided several appendices with additional details, definitions, and discussions for further context.

2. Data Sets and Methodology

All data were taken by the Parker Solar Probe (PSP; N. J. Fox et al. 2016) instruments. We use DC-coupled electric and magnetic field data from the PSP FIELDS instrument suite (S. D. Bale et al. 2016). The magnetic fields are sampled at ∼293 samples per second (sps) and the electric fields at ∼586 sps. The FIELDS instrument also has dynamic spectral radio data from ∼10 kHz to ∼20 MHz. All 3-vector parameters shown herein will be presented in radial, tangential, normal (RTN) coordinates (e.g., see M. Fränz & D. Harper 2002). The specifics of the electric field calibration are provided in Appendix C.

We use in situ thermal particle measurements from the SWEAP instrument suite (J. C. Kasper et al. 2016), specifically the SPAN-I detector (R. Livi et al. 2022). SPAN-I consists of an electrostatic analyzer (ESA) with a time-of-flight (TOF) mass discriminator to separate protons and alpha-particles. The detector measures 3D particle velocity distribution functions (VDFs). The ESA is a spherical top-hat allowing for an energy range of ∼a few eV to ∼30 keV and a total field-of-view (FOV) of $247.^{\circ}5 \times 120°$. The elevation angles ($\theta$) are defined by electrostatic deflectors at the entrance aperture, while azimuthal angles (ϕ) are defined by anodes below the microchannel plate (MCP) stack. The detector binned resolutions[12] are $\Delta E/E \sim 7\%$, $\Delta\phi \sim 11.^{\circ}25$–$22.^{\circ}5$, and $\Delta\theta \sim 15°$.

We use in situ energetic particle measurements from the IS⊙IS instrument suite (D. J. McComas et al. 2016). We specifically use the Energetic Particle Instruments, EPI-Lo and EPI-Hi (M. E. Hill et al. 2017; M. E. Wiedenbeck et al. 2017). For the ions, these measure energies ∼20 keV to ∼15 MeV nuc^{-1} and ∼1–200 MeV nuc^{-1}, respectively. Both detectors can differentiate particle species and we will focus on the protons herein. For electrons, EPI-Lo and EPI-Hi measure electrons with energies ∼20 keV to ∼1 MeV and ∼0.5–6 MeV, respectively. EPI-Lo and EPI-Hi have $\lesssim 30°$ and ∼45° angular resolutions, respectively. EPI-Lo and EPI-Hi have ∼11% and ∼8.3% energy resolution, respectively. EPI-Lo consists of 80 small apertures, covering nearly an entire hemisphere, while EPI-Hi features three telescopes that collectively provide five large FOV apertures.

The PSP spacecraft has a heat shield on its Sun-facing side to protect the instruments and bus from the extreme photon radiation it experiences during perihelion passes. Most of the instruments are hidden behind this heat shield to protect them. For instance, the SPAN-I FOV is occulted by the PSP heat shield. Near aphelion, the detector does not observe much of the core proton distribution. As the spacecraft approaches the Sun, its velocity transverse to the spacecraft-Sun line increases, aberrating the proton distribution into the SPAN-I FOV. Under some extreme conditions, the proton core can still move outside the SPAN-I FOV, even near perihelion (e.g., downstream of collisionless shock waves). When this happens, the velocity moments for the ions become less accurate. For the event studied herein, the proton core is fully covered upstream and partially occulted immediately downstream of the shock.

We also examined the energetic particle data from the 3DP instrument (R. P. Lin et al. 1995) on the Wind spacecraft (L. B. Wilson et al. 2021a). Specifically, we examined the solid state telescopes that measure electrons with energies ∼20–550 keV and protons with energies ∼70 keV to ∼7 MeV. We used these remote observations since Wind was close to the same Parker Spiral as PSP for this event.

[12] The intrinsic $\Delta\theta$ is at a higher resolution.

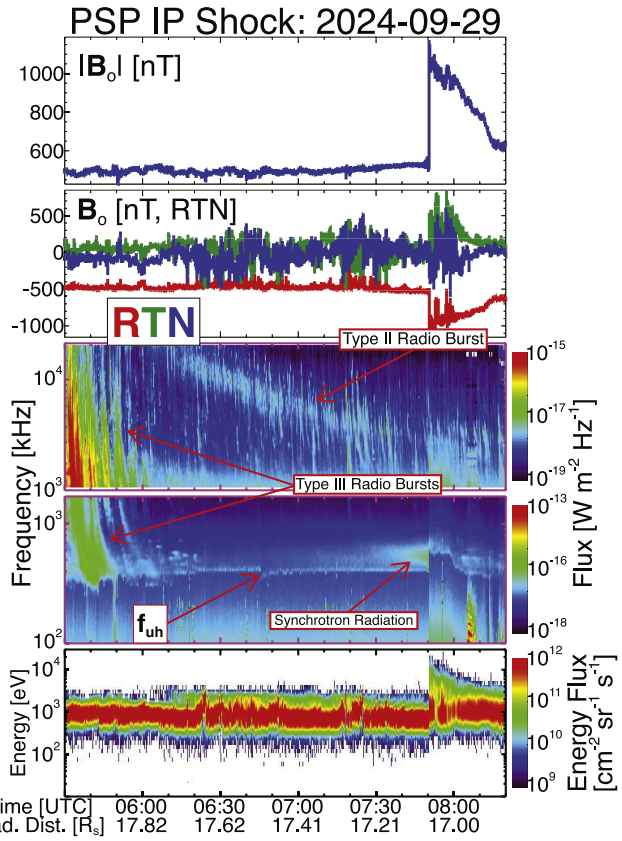

Figure 1. An overview of the IP shock observed on 2024 September 29. The panels show data in the following order from top to bottom: B_o [nT]; RTN components of $\boldsymbol{B}_o$ [nT]; dynamic radio spectra from the high frequency receiver (HFR) [W m^{-2}]; dynamic radio spectra from the low frequency receiver (LFR) [W m^{-2}]; and energy flux spectra from SPAN-I [eV cm^{-2} sr^{-1} s^{-1} eV^{-1}]. The HFR and LFR panels show some characteristic solar radio bursts and even some synchrotron radiation upstream of the shock (e.g., I. C. Jebaraj et al. 2024b).

3. Shock Overview

PSP encountered an IP shock on 2024 September 29 at ∼07:50:28.759 UTC at a solar radial distance of ∼17.07 R_s. The upstream and downstream time ranges used here to define asymptotic averages are 07:47:30.000–07:49:30.000 UTC and 07:51:20.000–07:51:50.000 UTC, respectively.

Figure 1 shows an overview of the FIELDS and SPAN-I FOV observations upstream of the IP shock (the IP shock is at the far right of the figure). The figure shows B_o and $\boldsymbol{B}_o$ in the top two panels, illustrating that the magnetic field is mostly radial. The next two panels show dynamic radio spectra observed by the electric field probes from ∼10 kHz to ∼20 MHz. We have provided some labels of interesting and relevant features for the reader.[13] The last panel shows the proton energy flux as a function of time and energy[14] to illustrate that at least for the upstream region, SPAN-I has good coverage of the proton VDF.

The relevant shock parameters are $\langle M_f \rangle_{\rm up} \sim$ 1.2, $\theta_{\rm Bn} \sim 50°$, and $\langle \beta_{\rm tot} \rangle_{\rm up} \sim$ 0.38 (see Appendix B for details). Thus, this IP shock is a low Mach number, low-beta, quasi-perpendicular shock as defined by L. B. Wilson et al. (2017). The density and magnetic compression ratios, $\bar{R}_n \sim$ 1.96 and $\bar{R}_B \sim$ 1.98, are small too.

The shock should also be subcritical to ion reflection, given that it does not exceed the first critical Mach number[15] (J. P. Edmiston & C. F. Kennel 1984; C. F. Kennel 1987). Further, there are no backstreaming, suprathermal ions observed by SPAN-I, but this may be due to its limited FOV.[16] There do appear to be many more energetic protons associated with this shock (see the discussion below and Figure 2), up to ∼1 MeV. Finally, we observe synchrotron radiation immediately upstream of the shock, which results from the acceleration of relativistic electrons (discussed below).

Following the same approach as I. C. Jebaraj et al. (2024b), we use the observed peak synchrotron frequencies between ∼485 and 610 kHz and the corresponding electron cyclotron frequencies ∼13.87–15.63 kHz (see Figure 1 and Appendix F) to get relativistic Lorentz factors between ∼5.6 and 6.6. These correspond to electron energies of ∼2.3–2.8 MeV. Note, however, that the total number of electrons need not be large to observe synchrotron emission (e.g., G. Mann et al. 2024). That is, there may be too few for the energetic particle instruments to observe (discussed below). The shock is not strongly oblique (i.e., $\theta_{\rm Bn}$ is not above 80°), which is thought to be more efficient for electron energization (e.g., M. M. Leroy & A. Mangeney 1984; C. S. Wu 1984; I. C. Jebaraj et al. 2023). We now examine the particle data to look for in situ measurements of energetic particles.

Figure 2 shows an overview of the energetic particle data from the Epi-Lo detector in the IS⊙IS instrument suite. The top panel, ChanE, is the Epi-Lo channel best suited to measure electrons. However, the ChanE detector is often contaminated with protons above ∼200 keV (e.g., see J. G. Mitchell et al. 2021, 2025). This is evidenced by the second panel, which shows that the number flux profiles of the 225 keV ChanP data follow the 90 keV ChanE data. The bottom panel shows the ChanP spectra, which measure protons. There are several things to note here. First, although we cannot quantifiably separate electrons from proton contamination in ChanE after ∼07:00 UTC, there are some differences which we can infer mean there are energetic electrons. However, the number flux is most likely very small. The similarities in the top and bottom panels also imply there is significant proton contamination. The presence of synchrotron emission supports the inference of energetic electrons as well and it is noted that there need not be a lot of energetic electrons to generate such an emission.

Perhaps more unexpected is the observation of protons from several 100 keV to more than 1 MeV upstream of this IP shock. We note that there is an inverse velocity arrival here, which tends to imply local energization at the shock rather than remote (e.g., G. C. Anagnostopoulos et al. 1986; E. T. Sarris et al. 1987; D. Caprioli & A. Spitkovsky 2014a, 2014b; D. Caprioli et al. 2015; A. Kouloumvakos et al. 2025). The abrupt cutoff immediately downstream of the shock ramp (i.e., around ∼07:50 UTC) in Figure 2 suggests that the particles are generated locally at the shock.[17] The reasons why

[13] $f_{\rm uh}$ is the upper hybrid resonance frequency and is defined in Appendix A

[14] The energies are from the detector midpoint energy bin values.

[15] $M_{\rm cr,1} \sim$ 2.21 for this shock.

[16] The data shown are for the forward-facing anodes (i.e., into the ram direction of the spacecraft trajectory). We also examined the backward-facing anodes but observed no evidence of backstreaming ions.

[17] Note that this data is from one of eight FOV "wedges" that looks sunward (i.e., particles coming from the shock), referred to as W3. The antisunward (not shown) wedge, W7, sees a dropout, but it occurs after that in W3 while the enhancement in W7 occurs during the W3 dropout. This implies the particles are leaving from both sides of the shock ramp. Given the magnetic field direction shown in 1, then W3 is roughly the parallel pitch-angle and W7 the antiparallel.

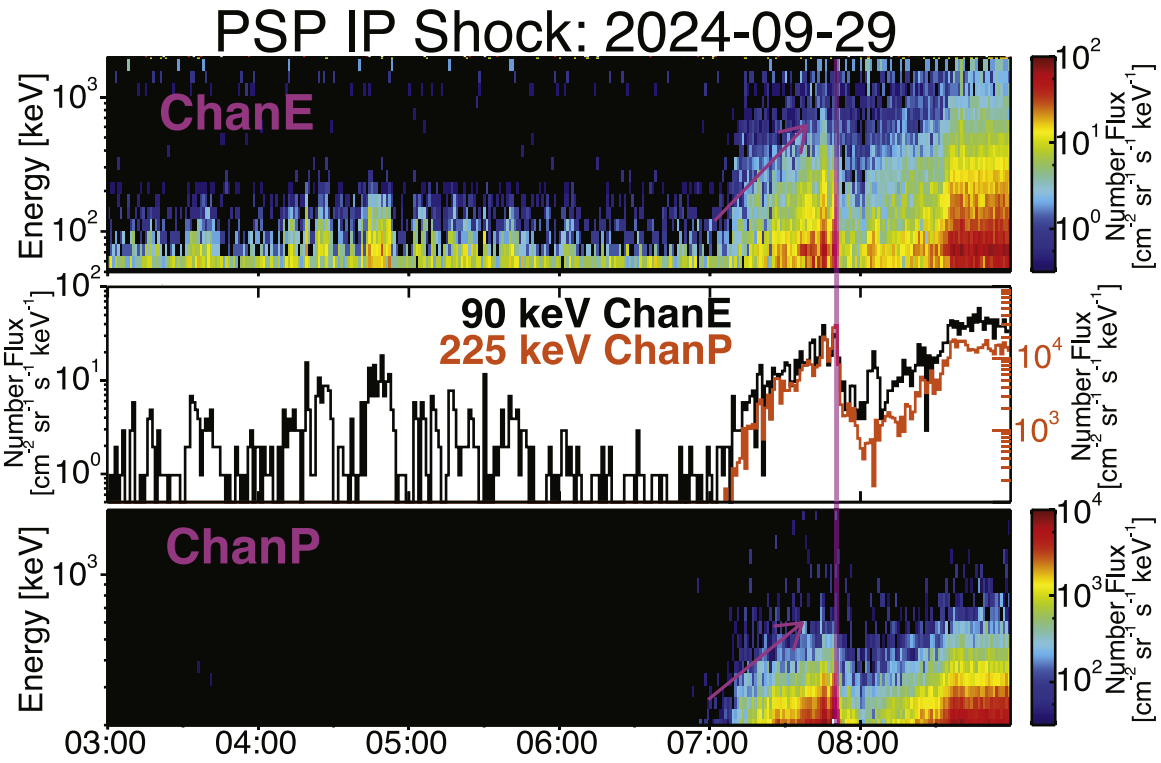

Figure 2. Observations of energetic particles from the Epi-Lo detector in the IS⊙IS instrument suite. The panels show data in the following order from top to bottom: number flux [cm^{-2} sr^{-1} s^{-1} keV^{-1}] spectra from ChanE; number flux [cm^{-2} sr^{-1} s^{-1} keV^{-1}] of the 90 keV ChanE energy bin (black line) and 225 keV ChanP energy bin (orange line); and number flux [cm^{-2} sr^{-1} s^{-1} keV^{-1}] spectra from ChanP. A vertical magenta line illustrates the shock crossing time and arrows help guide the eye to see the inverse velocity arrival in the particle data.

we argue for local versus remote energization are discussed below.

First, suppose the particles are energized in a remote location, either downstream or some transverse place along the shock surface. The shock ramp thickness of this IP shock was found to be ∼4.81 km. For reference, the gyroradii of ∼50–2000 keV electrons(∼200–2000 keV protons) in a ∼530 nT magnetic field are ∼1.44–15.6 km(∼120–390 km). One can see that the protons should be able to ballistically cross the shock at will and the higher energy electrons as well. Even in the downstream magnetic fields, the proton gyroradii at these energies are much larger than the shock ramp thickness. Thus, were the source downstream of the shock, we would not observe the abrupt cutoff just after the shock crossing. The much larger gyroradii than shock thickness also argues against a transverse location since the particles diffusing across the field would be observed downstream as well as upstream. One might also expect a regular energy dispersion (i.e., higher energy particles arrive before lower energies) if a remote source were responsible. However, the inverse velocity arrival could be due to differences in energization times for different energy particles (e.g., C. M. S. Cohen et al. 2024; T. M. Do et al. 2025; A. Kouloumvakos et al. 2025), which is suggested for diffusive shock acceleration. Yet this still would not explain why we observe the abrupt cutoff immediately downstream of the shock, given the large gyroradii of the particles.

Another scenario could be that the spacecraft crossed into another flux tube immediately downstream of the shock. The Fe/O and He/H ratios (not shown) are relatively stable through the shock until ∼1.5 hr further downstream near a heliospheric current sheet crossing, which does not support that hypothesis. Further, the proton pitch-angle distributions (not shown) show that particles near 180° (i.e., antiparallel to the magnetic field) arrive first time-wise. This is the antisunward direction upstream of the shock, consistent with the shock as the source and not consistent with an issue of magnetic field connection to the source.

We also observed energetic protons up to ∼4 MeV near 1 au with Wind[18] (not shown), as it was roughly along the same Parker Spiral as PSP for this event. We observed electrons up to several 100 keV as well with Wind, but similar to ChanE for Epi-Lo, the data suffer from proton contamination. Thus, it is difficult to quantifiably separate the two, but like Epi-Lo, there are differences suggesting there are electrons at Wind.

The part inconsistent with our current understanding of shock acceleration is that this is a weak, quasi-perpendicular shock. There is nothing extraordinary about the macroscopic shock parameters that would lead one to assume such a shock could generate MeV protons and electrons. For reference, mechanisms like shock drift acceleration should not generate protons in excess of ∼10 times the shock kinetic energy, or $\lesssim$10 keV for this event (e.g., D. Caprioli et al. 2015). The proton energies here are over 100 times this limit. This raises the question of why. Perhaps the extremely large amplitude whistler precursors seen upstream of the shock ramp (see Section 4) play an important role.

[18] Note that the ACE ULEIS (G. M. Mason et al. 1998) and STEREO-A IMPACT/SIT (G. M. Mason et al. 2008) both observed >100 keV nucleon^{-1} ^{4}He, oxygen, and iron. ACE ULEIS even observed a ^{3}He enhancement (not shown).

Table 1
Wave Parameters

Parameter	$X_{\min}$ [a]	$X_{5\%}$ [b]	$X_{25\%}$ [b]	$\bar{X}$ [c]	$\tilde{X}$ [d]	$X_{75\%}$ [b]	$X_{95\%}$ [b]	$X_{\max}$ [e]
Wave Normal Angles [deg]								
θ_{kB}	8.8	10	23	39	37	52	77	88
θ_{kV}	8.8	18	35	47	49	61	79	89
θ_{kn}	9.7	14	25	42	40	56	83	88
$\theta_{k\lambda}$	15	36	63	70	74	83	89	89
Rest-frame Parameters								
$\frac{k\ c}{\omega_{pe}}$	0.03	0.04	0.06	0.24	0.09	0.11	0.36	9.08
k [km^{-1}]	0.28	0.35	0.50	2.05	0.70	0.91	3.14	78
λ [km]	0.08	2.00	6.97	9.78	8.98	12.5	18.0	22.5
$\frac{\omega}{\Omega_{cp}}$	1.02	2.49	5.13	11.1	8.71	13.3	20.4	101
$\frac{\omega}{2\pi}$ [Hz]	8.21	20.0	41.2	89.5	70.0	107	164	809
$\frac{\omega}{k}$ [km s^{-1}]	40.9	189	438	594	587	757	905	1194

Notes. For symbol definitions, see Appendix A.
[a] minimum.
[b] jth percentile.
[c] mean.
[d] median.
[e] maximum.

4. Wave Analysis

In this section, we introduce and discuss how we filter the field data and then calculate amplitudes and Poynting fluxes. The software used to analyze the intervals is publicly available and has been used in previous refereed publications (e.g., L. B. Wilson 2022).

4.1. Minimum Variance Analysis

In this section, we introduce and discuss how we filter the fluxgate data and then analyze it using minimum variance analysis (MVA; e.g., A. V. Khrabrov & B. U. Ö. Sonnerup 1998).

The MVA details are described in previous work (e.g., L. B. Wilson et al. 2017; S. Giagkiozis et al. 2018) and in Appendix D. We performed MVA on filtered and detrended magnetic field data, and a whistler precursor was observed between ∼07:50:27.500 UTC and ∼07:50:28.751 UTC. There were 181 unique MVA solutions, of which 102 satisfied our eigenvalue ratio criteria. We also computed the various wave normal angles, θ_{kj}, as the acute angles between the wave normal unit vectors, $\hat{\boldsymbol{k}}$, and other vectors of interest.[19] The one-variable statistics of these wave normal angles are shown in Table 1.[20] We also show the wavenumber, k, wavelength, λ, rest-frame frequency, ω, and rest-frame phase speed, $V_{ph}=\frac{\omega}{k}$ in Table 1.

The wave normal angles are consistent with previous studies examining whistler precursors in that they find the waves propagate obliquely with respect to the shock normal, the upstream magnetic field, and they are not always in the same plane as these two vectors (i.e., the shock is intrinsically three dimensional) (e.g., L. B. Wilson et al. 2009, 2012, 2017; A. J. Hull et al. 2012, 2020, 2024). Both the 3D nature of collisionless shocks and the wave normal angles are important for simulations and modeling efforts, which are computationally limited, making full 3D fully kinetic simulations extremely difficult.

We have now $\hat{\boldsymbol{k}}$ and θ_{kj} from MVA; therefore, we can approximate the rest-frame parameters following the approach by L. B. Wilson et al. (2013) and L. B. Wilson et al. (2017; see details in Appendix D). That is, we Doppler-shift the cold plasma whistler dispersion relation[21] and invert to find the relevant rest-frame parameters, whose one-variable statistics are shown in Table 1.

The normalized parameters and wave normal angles are all consistent with precursors observed at IP shocks near 1 au (e.g., L. B. Wilson et al. 2009, 2012, 2013, 2017) and precursors upstream of the terrestrial bow shock (e.g., A. J. Hull et al. 2012, 2020, 2024; L. B. Wilson et al. 2014a, 2014b; L. B. Wilson 2016). These are on the lower end of the normalized frequency range, but it is clear from Figure 3 (introduced and discussed in Section 4.2) that even at ∼293 sps, the fluxgate data is underresolving the precursor. Cursory examination of the search coil dynamic spectra (not shown) indicates there are higher-frequency whistlers upstream and within the precursor, which is also consistent with previous observations (e.g., A. J. Hull et al. 2012, 2020, 2024; L. B. Wilson et al. 2012, 2013, 2014a, 2014b). We also examined the search coil time series data (D. M. Malaspina et al. 2016) because the fluxgate does not fully resolve the waveform (i.e., the search coil has a higher sample rate). The search coil amplitudes are similar to those of the fluxgate; thus, it did not noticeably underestimate the magnetic amplitude.

[19] i.e.,., $\langle \boldsymbol{B}_o \rangle_{up}$, $\langle \boldsymbol{V}_{bulk} \rangle_{up}$, $\hat{\boldsymbol{n}}_{sh}$, and a latitude vector that is the cross-product between $\hat{\boldsymbol{n}}_{sh}$ and $\langle \boldsymbol{B}_o \rangle_{up}$.

[20] Note that the distribution of values is not Gaussian, so we use percentiles instead of standard deviation or variance.

[21] Note that D. Stansby et al. (2016) illustrated that for small k(large wavelength), the cold plasma whistler dispersion relation matches observations quite well.

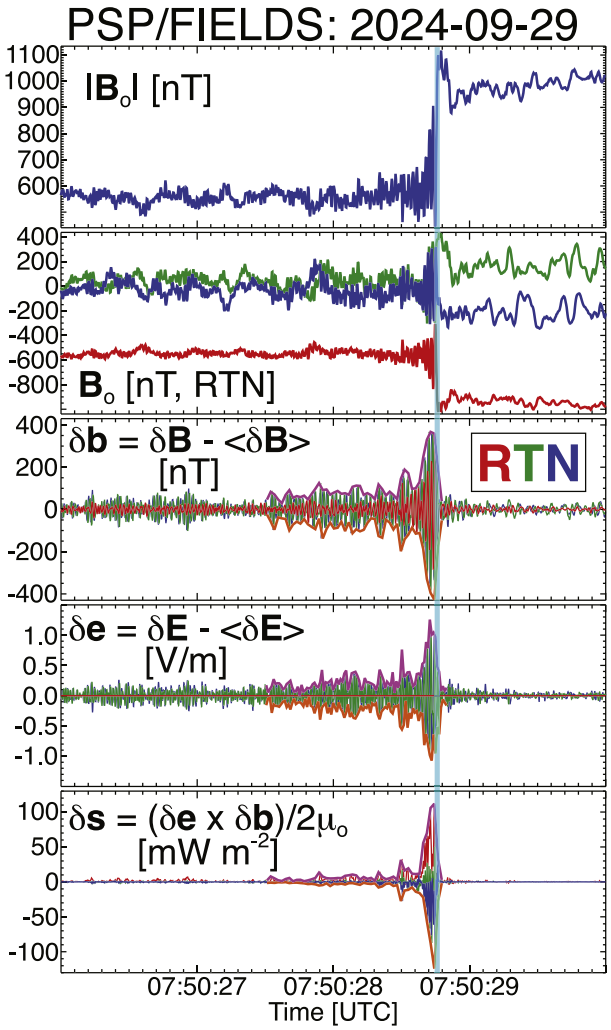

Figure 3. Illustration of the analysis performed on the whistler precursor upstream of the IP shock observed on 2024 September 29. The panels show data in the following order from top to bottom: B_o [nT]; RTN components of $\boldsymbol{B}_o$ [nT]; filtered and detrended $\boldsymbol{B}_o$ [nT]; filtered and detrended $\boldsymbol{E}_o$ [mV/m]; and the Poynting flux resulting from the data in the previous two panels [mW m^{-2}].

In summary, the approximated rest-frame parameters are consistent with previous estimates for fast/magnetosonic-whistler precursor waves.

4.2. Amplitude Statistics

In this section, we discuss the amplitudes of the whistler precursors (additional details can be found in Appendix E and symbols are defined in Appendix A).

Figure 3 shows the time series of the fields with the outer envelope around the filtered and detrended magnetic field, $\delta\boldsymbol{b}$, electric field, $\delta\boldsymbol{e}$, and Poynting flux,[22] $\delta\boldsymbol{s}$, to determine the peak-to-peak (pk–pk) wave amplitude.[23] This follows from the method described in L. B. Wilson et al. (2017). The shock is propagating away from the Sun, so the positive R-component of $\delta\boldsymbol{s}$ illustrates that the precursor's group velocity is directed upstream, consistent with previous observations at low Mach number shocks (e.g., D. Sundkvist et al. 2012; A. P. Dimmock et al. 2022). Note this can be in contrast to some observations at higher Mach number shocks (e.g., L. B. Wilson et al. 2012; A. P. Dimmock et al. 2013; A. J. Hull et al. 2020, 2024).

We performed one-variable statistics on the outer envelope of $\delta\boldsymbol{b}$, $\delta\boldsymbol{e}$, and $\delta\boldsymbol{s}$ shown in the third, fourth, and fifth panels of Figure 3. There are 47 time stamps for $\delta\boldsymbol{b}$ and $\delta\boldsymbol{s}$ and 97 time stamps for $\delta\boldsymbol{e}$. From these, we calculate the pk–pk wave amplitudes, $\delta b_{\rm pk-pk}$, $\delta e_{\rm pk-pk}$, and $\delta s_{\rm pk-pk}$. The one-variable statistics of these wave amplitudes are shown in Table 2.

There are several important takeaways from the statistics shown in Table 2. The first is that this is the largest amplitude whistler precursor ever recorded, with a maximum $\delta b_{\rm pk-pk} \sim 786$ nT. The largest amplitude precursor upstream of an IP shock observed at 1 au is $\delta b_{\rm pk-pk} \sim 13$ nT (e.g., L. B. Wilson et al. 2017), i.e., over 60 times smaller in amplitude and over 3600 times smaller in energy density.[24] Interestingly, the maximum values for $\frac{\delta b_{\rm pk-pk}}{\langle B_o\rangle_{\rm up}}$ and $\frac{\delta b_{\rm pk-pk}}{\Delta \vec{B}_o}$ are smaller for the PSP precursor than the maximum observed for 1 au shocks. The maximum PSP to the maximum 1 au values are ∼0.93 and ∼0.09, respectively. Note that more typical 1 au values are $\delta b_{\rm pk-pk} \sim$ 0.3 nT, $\frac{\delta b_{\rm pk-pk}}{\langle B_o\rangle_{\rm up}} \sim$ 0.04, and $\frac{\delta b_{\rm pk-pk}}{\Delta \vec{B}_o} \sim$ 0.06.

The first thing to note about the electric fields is that $\delta e_{\rm pk-pk}$ ranges from $\sim$100 mV m^{-1} to $>$2000 mV m^{-1} for the precursor, which is ∼10–200 times larger than any previous electric field measurement of whistler precursors (e.g., A. J. Hull et al. 2012, 2020, 2024; D. Sundkvist et al. 2012; L. B. Wilson et al. 2014b, 2021b). Using the range of wavelengths from Section 4.1, we can get a rough estimate of the electric potential across the oscillations of the wave. The range of values is ∼540–28,050 volts. Precursors upstream of shocks near Earth tend to directly affect electrons in the ∼0.1–1.0 keV range (e.g., L. B. Wilson et al. 2012; M. Oka et al. 2019; A. J. Hull et al. 2020). If this precursor can directly affect electrons up to ∼28 keV that would greatly alter the particle dynamics of the shock from what one would expect for a laminar transition. That is, the particle dynamics would be significantly different in the absence of the precursor.

The next thing to note is that the peak $\delta s > 200$ mW m^{-2}, which is nearly 2000 times larger than the largest whistler precursor measurements at the terrestrial bow shock (e.g., D. Sundkvist et al. 2012; L. B. Wilson et al. 2014b; A. J. Hull et al. 2020, 2024). In fact, this is nearly 100 times larger than the largest Poynting flux measured at a collisionless shock to date (e.g., L. B. Wilson et al. 2014b). For context, these Poynting fluxes are >200 times what is necessary to drive the terrestrial aurora (e.g., J. R. Wygant et al. 2000; V. Angelopoulos et al. 2002). Further, the area over which the aurora is active is much smaller than the surface of the shock; thus, the total energy of the whistler precursors is far greater.

We compared the wave magnetic energy density, P_{wB}, to the upstream proton thermal, $P_{\rm Tp}$, proton ram, $P_{\rm rp}$, and magnetic energy densities, P_{Bo}, to those at 1 au. We start with typical 1 au plasma parameters taken from L. B. Wilson et al. (2021a) and L. B. Wilson et al. (2023). That is, we use $B_o \sim 5.04$ nT, $T_p \sim 4.23$ eV, $V_p \sim 405$ km s^{-1}, and $n_p \sim 5.24$ cm^{-3}. The 1 au precursor amplitudes are taken from L. B. Wilson et al. (2017), where the minimum, median, and maximum are 0.2 nT,

[22] Note that we only fully determine the R-component of $\delta\boldsymbol{s}$, with partial values for the T- and N-components.

[23] We use the peak-to-peak amplitude because the wave oscillations are not symmetric about a mean value. If the reader prefers the more common wave amplitude, the peak-to-peak values can be divided by 2.

[24] Note that the median peak amplitudes for 1 au precursors are only 2.3 nT, which is over 340 times smaller than the precursor examined herein, or over 100,000 times smaller in energy density.

Table 2
Wave Amplitudes

Parameter	X_{min}[a]	$X_{5\%}$[b]	$X_{25\%}$[b]	$\bar{X}$[c]	$\tilde{X}$[d]	$X_{75\%}$[b]	$X_{95\%}$[b]	X_{max}[e]
Wave Magnetic Field								
δb_{pk-pk} [nT]	70	85	127	214	168	229	659	786
$\frac{\delta b_{pk-pk}}{\langle B_o\rangle_{up}}$	0.13	0.16	0.24	0.40	0.32	0.43	1.24	1.48
$\frac{\delta b_{pk-pk}}{\Delta \vec{B}_o}$	0.12	0.14	0.21	0.36	0.29	0.39	1.12	1.33
Wave Electric Field								
δe_{pk-pk} [mV/m]	103	140	300	545	418	660	1593	2240
$\frac{\delta e_{pk-pk}}{\langle E_o\rangle_{up}}$	7.21	9.84	21.0	38.2	29.3	46.2	112	157
Wave Poynting Flux								
δs_{pk-pk} [mW m^{-2}]	2.07	2.92	6.79	25.2	8.90	19.6	126	236
$\frac{\delta s_{pk-pk}}{\langle S_o\rangle_{up}}$	0.69	0.98	2.27	8.42	2.97	6.54	42.0	78.9

Notes. For symbol definitions, see Appendix A.
[a] minimum.
[b] jth percentile.
[c] mean.
[d] median.
[e] maximum.

2.3 nT, and 13 nT. The corresponding PSP values are given above and in Section 3. The one-variable statistics of these normalized wave amplitudes are shown below as X_{min}–$X_{max}(\tilde{X})$:

1 *au IP shocks*
- $P_{wB}/P_{Tp} \sim$ 0.004–19(0.59)
- $P_{wB}/P_{rp} \sim$ 0.00002–0.09(0.003)
- $P_{wB}/P_{Bo} \sim$ 0.002–6.7(0.21)

PSP event
- $P_{wB}/P_{Tp} \sim$ 0.16–21(0.93)
- $P_{wB}/P_{rp} \sim$ 0.01–1.1(0.05)
- $P_{wB}/P_{Bo} \sim$ 0.02–2.2(0.10)

Ratio of PSP event to 1 au shocks[25]
- $P_{wB}/P_{Tp} \sim$ 36–1.1(1.6)
- $P_{wB}/P_{rp} \sim$ 404–11(17)
- $P_{wB}/P_{Bo} \sim$ 12–0.48(0.33)

Normalizing the wave energy density to background plasma conditions illustrates that compared to the ambient thermal and ram energy densities, the PSP precursor is unusually large. This is even compared to the largest precursors seen at 1 au. The median values are larger by ∼60% for P_{wB}/P_{Tp} and ∼1700% for P_{wB}/P_{rp}. The latter is easily explained as the solar wind speed does not change by more than ∼50% between ∼17 R_s and ∼200 R_s, but the ambient number density decreases by nearly 3 orders of magnitude. That the wave has so much more energy density compared to the ambient ram energy density for the PSP event than even the strongest 1 au events is surprising, given the PSP shock is on the weaker end of the range of values defined as low Mach number by L. B. Wilson et al. (2017). That is, a zeroth-order approximation would argue that higher Mach number shocks have larger amplitude fluctuations since they have more free energy to dissipate. Thus, one may expect even larger absolute and normalized wave amplitudes for higher Mach number shocks observed by PSP within 20 R_s of the Sun.

In summary, the absolute amplitude of this precursor is by far the largest ever recorded. The wave energy densities normalized to the upstream magnetic field energy density may be comparable to many IP shocks observed near 1 au (e.g., see statistics in L. B. Wilson et al. 2017), but the ratios with respect to thermal and ram energy densities are much larger.[26] The absolute wave amplitudes are orders of magnitude larger than typical 1 au precursors, whether one looks at magnetic field, electric field, or Poynting flux. In fact, the peak Poynting flux for this precursor is >200 times what is necessary to drive the terrestrial aurora. This may explain why such a weak, mildly oblique shock appears to generate such highly energetic particles.[27]

5. Discussion

We present observations of an IP shock at ∼17 R_s from the Sun observed by PSP on 2024 September 29 at ∼07:50:28.759 UTC. The shock is found to exhibit evidence of energetic particle enhancements upstream from synchrotron emission. This is particularly important given that we estimate the shock is rather weak. That is, this is a low Mach number ($\langle M_f\rangle_{up}\sim$ 1.2), quasi-perpendicular ($\theta_{Bn}\sim 50°$), low-beta ($\langle\beta_{tot}\rangle_{up}\sim 0.38$) shock. It was also found to be subcritical to the first critical Mach number and all the whistler critical Mach numbers. Decades of shock acceleration literature have argued that such shock should not be capable of generating particles

[25] These are direct ratios of the above values, so the X_{min}–X_{max} may not show low to high values.

[26] The ram energy density will not change much between PSP and 1 au but the wave energy is much higher at PSP. The thermal energy density appears to decrease more slowly than the wave energy density out to 1 au.

[27] Inferred from synchrotron radiation and observed in IS⊙IS at PSP and with Wind 3DP near Earth. The 3DP data showed weak regular energy dispersion in 3DP protons, which suggests significant scattering in transit.

with energies $\gtrsim$1000 times the ambient thermal energies (e.g., see discussion in C. F. Kennel et al. 1985; R. A. Treumann 2009, and references therein). Yet we observe synchrotron emission and energetic particles upstream of the shock. We even observe energetic protons up to ∼4 MeV near 1 au with Wind and >100 keV nucleon^{-1} ^{4}He, oxygen, and iron with ACE and STEREO-A.

This is a weak and otherwise uninteresting IP shock, based upon macroscopic shock parameters alone. Such a shock should only generate protons with, at most, ∼10 times the shock kinetic energy, or $\lesssim$10 keV for this event (e.g., D. Caprioli et al. 2015). It is so weak, the standard shock acceleration mechanisms (i.e., shock drift acceleration, Fermi acceleration, etc.) cannot explain MeV electrons or protons. What makes this shock special/different from the dozens of shocks observed near 1 au with similar parameters? The first thing we noticed was the extremely large amplitude whistler precursor. The normalized precursor wave parameters are similar to 1 au IP shock whistler precursors (i.e., similar normalized frequencies and wavenumbers), but the absolute amplitudes are 1 to several orders of magnitude larger than typical 1 au IP shocks. The magnetic field amplitudes are over 60 times larger (i.e., over 3600 times larger in energy density), electric fields are over ∼10–200 times larger (i.e., ∼100–40000 times more energy density), and the Poynting fluxes are nearly 2000 times larger. In fact, the Poynting fluxes are >200 times what is necessary to drive the terrestrial aurora (e.g., J. R. Wygant et al. 2000; V. Angelopoulos et al. 2002).

The whistler precursor amplitudes are, of course, larger in part because the quasi-static field magnitude has increased. Thus, we normalized them properly to provide context for the amplitudes. We calculated the wave magnetic energy density relative to the upstream thermal proton, proton ram, and magnetic field energy densities. The PSP whistlers are similar to or smaller than 1 au whistler precursors when normalized to the upstream magnetic field energy densities. However, when we normalized to the thermal and ram energy densities, the PSP whistler precursor is tens to thousands of percent larger than typical 1 au whistler precursors. Thus, even the normalized amplitudes can be much larger than typical 1 au whistler precursors.

The observation of MeV energy particles upstream of the shock with inverse velocity arrival, a sharp cutoff at the shock, and synchrotron emission all support this shock somehow producing energetic particles (detailed justification given in Section 3). The only clear outlier is the whistler precursor. Recent work (S. Raptis et al. 2025; X. Shi et al. 2025) has revealed that the standard shock acceleration mechanisms alone cannot reproduce the observed particle spectral slope or energy range without the inclusion of fluctuations like whistler precursors. That work was focused on the terrestrial foreshock near 1 au. The larger amplitude fluctuations observed here are likely to generate a higher maximum energy for accelerated particles.

These observations have important implications for our understanding of particle energization at collisionless shocks. The current paradigm is that weak shocks such as the one discussed herein should not be capable of generating energetic particles. Yet we observe them. This raises several interesting questions about the partition of energy. If one generates enough energetic particles or a few with high enough energies, one can regulate the shock energy budget alone through these particles (e.g., cosmic-ray mediated shocks) (e.g., D. Caprioli & A. Spitkovsky 2013).

More puzzling is what these observations imply for more extreme environments where the ambient magnetic fields are much larger. Following the same scaling we observe throughout the heliosphere (i.e., $\delta b_{\rm pk-pk}/\langle B_o\rangle_{\rm up}$∼0.2–1.2) but extrapolating to a more extreme environment, one could expect to observe $\langle B_o\rangle_{\rm up} > 10^{17}$ nT for pulsars and/or magnetars (e.g., A. Stepanov et al. 2011; A. V. Stepanov & V. V. Zaitsev 2013). That is ∼14 orders of magnitude larger than the field upstream of this IP shock, or ∼28 orders of magnitude more energy density in a similar fluctuation. The whistler precursors presented herein are more than 10 times larger in amplitude than those observed near 1 au and the electron energies (inferred from synchrotron emission) are roughly 10 times higher than those observed in the terrestrial foreshock. If that scaling held, one would expect to see EeV energy electrons near magnetars.[28] This is a gross oversimplification. However, we make this point and scaling argument to illustrate the potential differences in the current, maximum expected energies for some extreme environments.

6. Summary

In summary, we have observed evidence of 100 s of keV to >MeV energy particle enhancements upstream of an IP shock using PSP data. The macroscopic shock parameters show it is a very weak, quasi-perpendicular shock, which is not expected to generate such energetic particles. We observe an extremely large amplitude whistler precursor upstream of the shock, which has energy densities tens to thousands of percent larger than typical 1 au whistler precursors, when normalized to the ram or thermal energy densities. We infer that this whistler precursor is playing an important role in the energization of these particles.

Future work will take a comprehensive look at more weak, near-Sun IP shocks to determine the frequency of energetic particle enhancements. Future work will also make use of PSP's recent closest approach, with perihelia remaining at the same distance throughout the rest of the mission, to study IP shocks even closer to the Sun.

Acknowledgments

Analysis software (L. B. Wilson 2022) used herein can be found on GitHub.[29]and referenced in V. Angelopoulos et al. (2019). All ACE, Wind, and STEREO data discussed herein are available through SPDF/CDAWeb.[30] PSP was designed, built, and is now operated by the Johns Hopkins Applied Physics Laboratory as part of NASA's Living With a Star (LWS) program (contract NNN06AA01C). Support from the LWS management and technical team has played a critical role in the success of the PSP mission. The FIELDS experiment was developed and is operated under NASA contract NNN06AA01C. J.S.H., S.D.B., D.M.M., C.M.S.C., R.L., M. L.S., and A.S. are supported through PSP contracts. All PSP data were provided by the instrument teams and are soon to be released for public archival at SPDF/CDAWeb. J.G.M. acknowledges the support of the NASA PSP grant

[28] This is ignores radiative losses and many other factors like inverse Compton scattering, etc.
[29] https://github.com/lynnbwilsoniii/wind_3dp_pros
[30] https://cdaweb.gsfc.nasa.gov

NNN06AA01C. I.C.J. is grateful for support by the Research Council of Finland (SHOCKSEE, grant No. 346902), and the European Union's (EU's) Horizon 2020 research and innovation program under grant agreement No. 101134999 (SOLER). The study reflects only the authors' view and the European Commission is not responsible for any use that may be made of the information it contains. I.C.J. was also supported by the International Space Science Institute (ISSI) in Bern through ISSI International Team project No. 23-575, "Collisionless Shock as a Self-Regulatory System" and through the Visiting Scientist program. A.K. acknowledges financial support from NASA NNN06AA01C (PSP EPI-Lo) contract and NASA's HGIO grant 80NSSC24K0555. G.D.B. acknowledges the support of the IS⊙IS instrument suite on NASA's PSP Mission, contract NNN06AA01C. D.M.M. acknowledges the support of the NASA PSP grant NNN06AA01C.

Appendix A
Definitions

In this appendix, the symbols and notation used throughout will be defined. For all direction-dependent parameters, we use the subscript j to represent the direction, where $j =$ tot for the entire distribution, $j = \parallel$ for the parallel direction, and $j = \perp$ for the perpendicular direction, where parallel/perpendicular is with respect to the quasi-static magnetic field vector, $\boldsymbol{B}_o$ [nT]. Below are the symbol/parameter definitions:

1. *Acronyms, initialisms, and symbols*
   - PSP ≡ Parker Solar Probe
   - VDF ≡ velocity distribution function
   - SCF ≡ spacecraft rest frame
   - SHF ≡ shock rest frame
   - PRF ≡ plasma rest frame
   - ESA ≡ electrostatic analyzer
   - MCP ≡ microchannel plate
   - TOF ≡ time-of-flight
   - FOV ≡ field-of-view
   - IP ≡ interplanetary
2. *One-variable statistics*
   - $X_{\min} \equiv$ minimum
   - $X_{\max} \equiv$ maximum
   - $\bar{X} \equiv$ mean
   - $\tilde{X} \equiv$ median
   - $X_{y\%} \equiv$ yth percentile
3. *Fundamental parameters*
   - $\varepsilon_o \equiv$ permittivity of free space
   - $\mu_o \equiv$ permeability of free space
   - $c \equiv$ speed of light in vacuum [km s^{-1}] $= (\varepsilon_o\ \mu_o)^{-1/2}$
   - $k_B \equiv$ the Boltzmann constant [J K^{-1}]
   - $e \equiv$ the fundamental charge [C]
   - $R_s \equiv$ mean solar radius [km]
4. *Plasma parameters*
   - $n_s \equiv$ the number density [cm^{-3}] of species s
   - $m_s \equiv$ the mass [kg] of species s
   - $Z_s \equiv$ the charge state of species s
   - $q_s \equiv$ the charge [C] of species $s = Z_s e$
   - $T_{s,j} \equiv$ the scalar temperature [eV] of the jth component of species s
   - $V_{\mathrm{Ts},j} \equiv$ the most probable thermal speed [km s^{-1}] of a one-dimensional velocity distribution (see Equation (A1aa))
   - $\Omega_{cs} \equiv$ the angular cyclotron frequency [rad s^{-1}] (see Equation (A1bb))
   - $\omega_{ps} \equiv$ the angular plasma frequency [rad s^{-1}] (see Equation (A1c))
   - $\lambda_{De} \equiv$ the electron Debye length [m] (see Equation (A1d))
   - $\rho_{cs} \equiv$ the thermal gyroradius [km] (see Equation (A1eee))
   - $\lambda_s \equiv$ the inertial length [km] (see Equation (A1f))
   - $\beta_{s,j} \equiv$ the plasma beta [unitless] of the jth component of species s (see Equation (A1g))
   - ω_{uh} $(= 2\pi f_{uh}) \equiv$ the angular upper hybrid resonance frequency [rad s^{-1}] (see Equation (A1h))
   - $\boldsymbol{E}_o \equiv$ the convective electric field [mV/m] $= -\boldsymbol{V}_{\mathrm{bulk}} \times \mathbf{B}_o$
   - $\boldsymbol{S}_o \equiv$ quasi-static Poynting flux [mW m^{-2}] $= \boldsymbol{E}_o \times \boldsymbol{B}_o / 2\mu_o$
   - $\delta\boldsymbol{q} \equiv$ measured field 3-vector (i.e., electric, magnetic, or Poynting flux) that has been filtered and/or detrended to remove DC offsets
   - $L_{\mathrm{eff}} \equiv$ the effective antenna length of the PSP FIELDS electric field instrument (see Appendix C for details)
   - $f_{\mathrm{sync}} \equiv$ peak frequency [Hz] of the observed synchrotron emission (see Appendix F for details)
5. *Shock parameters*
   - $\langle Q \rangle_j \equiv$ the average of parameter Q over the jth shock region, where $j =$ up or dn
   - $\Delta\bar{Q} = \langle Q \rangle_{\mathrm{dn}} - \langle Q \rangle_{\mathrm{up}} \equiv$ the change in the asymptotic average of parameter Q over the jth shock region
   - $\bar{R}_n = \langle n_e \rangle_{\mathrm{dn}} / \langle n_e \rangle_{\mathrm{up}} \equiv$ the average shock density compression ratio [unitless]
   - $\bar{R}_B = \langle B_o \rangle_{\mathrm{dn}} / \langle B_o \rangle_{\mathrm{up}} \equiv$ the average shock magnetic field compression ratio [unitless]
   - $C_s \equiv$ the sound or ion-acoustic sound speed [km s^{-1}] (see Equation (A1i))
   - $V_A \equiv$ the Alfvén speed[31] [km s^{-1}] (see Equation (A1j))
   - $V_{\mathrm{ms}} \equiv$ the magnetosonic speed [km s^{-1}] (see Equation (A1k))
   - $V_f \equiv$ the fast mode speed [km s^{-1}] (see Equation (A1l))
   - $\boldsymbol{n}_{\mathrm{sh}} \equiv$ the shock normal unit vector [unitless]
   - $\theta_{\mathrm{Bn}} \equiv$ the shock normal angle[32] [deg]
   - $\langle V_{\mathrm{shn}} \rangle_j \equiv$ the jth region average shock normal speed [km s^{-1}] in the spacecraft frame
   - $\langle U_{\mathrm{shn}} \rangle_j = [\langle \boldsymbol{V}_{\mathrm{bulk}} \rangle_j - (V_{\mathrm{shn}}\ \ \boldsymbol{n}_{\mathrm{sh}})] \cdot \boldsymbol{n}_{\mathrm{sh}} \equiv$ the jth region average shock normal speed [km s^{-1}] in the shock rest frame[33] (i.e., the speed of the flow relative to the shock)
   - $\langle M_A \rangle_j \equiv$ the jth region average Alfvénic Mach number [unitless] $= \langle |U_{\mathrm{shn}}| \rangle_j / \langle V_A \rangle_j$
   - $\langle M_{Cs} \rangle_j \equiv$ the jth region average sonic Mach number [unitless] $= \langle |U_{\mathrm{shn}}| \rangle_j / \langle C_s \rangle_j$
   - $\langle M_f \rangle_j \equiv$ the jth region average fast mode Mach number [unitless] $= \langle |U_{\mathrm{shn}}| \rangle_j / \langle V_f \rangle_j$
   - $M_{\mathrm{cr},1} \equiv$ the first critical Mach number [unitless]
   - $M_{\mathrm{ww}} \equiv$ the linear whistler (phase) Mach number [unitless]
   - $M_{\mathrm{gr}} \equiv$ the linear whistler (group) Mach number [unitless]
   - $M_{\mathrm{nw}} \equiv$ the nonlinear whistler Mach number [unitless]

The first critical Mach number is defined in J. P. Edmiston & C. F. Kennel (1984) and C. F. Kennel (1987), while

[31] We only use contributions from protons as we do not yet have good alpha-particle moments.

[32] The acute reference angle between $\langle \boldsymbol{B}_o \rangle_{\mathrm{up}}$ and $\boldsymbol{n}_{\mathrm{sh}}$.

[33] Note that both $\langle V_{\mathrm{shn}} \rangle_j$ and $\langle U_{\mathrm{shn}} \rangle_j$ are signed quantities (i.e., they need not be positive definite) but we report the absolute values for simplicity.

the three whistler critical Mach numbers are defined in V. V. Krasnoselskikh et al. (2002). The variables that rely upon multiple parameters are given in the following equations:

$$V_{Ts,j} = \sqrt{\frac{2 \quad k_{\rm B} \quad T_{s,j}}{m_s}} \tag{A1a}$$

$$\Omega_{cs} = \frac{q_s \quad B_o}{m_s} \tag{A1b}$$

$$\omega_{\rm ps} = \sqrt{\frac{n_s \quad q_s^2}{\varepsilon_o \quad m_s}} \tag{A1c}$$

$$\lambda_{\rm De} = \frac{V_{\rm Te,tot}}{\sqrt{2} \quad \omega_{\rm pe}} = \sqrt{\frac{\varepsilon_o \quad k_{\rm B} \quad T_{e,\rm tot}}{n_e \quad e^2}} \tag{A1d}$$

$$\rho_{cs} = \frac{V_{\rm Ts,tot}}{\Omega_{cs}} \tag{A1e}$$

$$\lambda_s = \frac{c}{\omega_{\rm ps}} \tag{A1f}$$

$$\beta_{s,j} = \frac{2\mu_o n_s k_B T_{s,j}}{|\boldsymbol{B}_o|^2} \tag{A1g}$$

$$\omega_{\rm uh}^2 = \omega_{\rm pe}^2 + \Omega_{\rm ce}^2 \tag{A1h}$$

$$C_s = \sqrt{\frac{k_{\rm B}(Z_i \quad \gamma_e \quad T_{e,\rm tot} + \gamma_i \quad T_{i,\rm tot})}{m_i + m_e}} \tag{A1i}$$

$$V_{\rm A} = \frac{|\boldsymbol{B}_o|}{\sqrt{\mu_o \quad m_i \quad n_i}} \tag{A1j}$$

$$V_{\rm ms} = \sqrt{C_s^2 + V_{\rm A}^2} \tag{A1k}$$

$$V_f = \left[\frac{V_{\rm ms}^2 + \sqrt{V_{\rm ms}^2 - 4 \quad C_s^2 \quad V_{\rm A}^2 \quad \cos^2\theta}}{2}\right]^{1/2} \tag{A1l}$$

where, herein, we use $Z_i\gamma_e = 1$, $\gamma_i = 3$, $m_i = m_p$, and θ ($\rightarrow\theta_{\rm Bn}$) is the shock normal angle of propagation for any V_f calculation.

Appendix B
Shock Parameters

In this appendix, we explain how we calculated the relevant shock parameters then list them.

The SPAN-I FOV was partially occulted downstream of this IP shock greatly reducing the quality and accuracy of the velocity moments. We need $\boldsymbol{V}_{\rm bulk}$ in the downstream, so we examined the energy flux spectra from SPAN-I to find the peak in energy flux versus time. Three data products are available for energy flux spectra: energy, elevation, and azimuth. Using these three values, we can determine $\boldsymbol{V}_{\rm bulk}$ in instrument coordinates, then rotate to RTN coordinates. We need $\langle\boldsymbol{V}_{\rm bulk}\rangle_{\rm up}$ and $\langle\boldsymbol{V}_{\rm bulk}\rangle_{\rm dn}$ to calculate parameters like $\langle|V_{\rm shn}|\rangle_{\rm up}$ and $\langle|U_{\rm shn}|\rangle_{\rm up}$, which are required to calculate the relevant Mach numbers. We use the peak in the energy flux spectra for both $\langle\boldsymbol{V}_{\rm bulk}\rangle_{\rm up}$ and $\langle\boldsymbol{V}_{\rm bulk}\rangle_{\rm dn}$ throughout.

To determine the shock normal unit vector, we used the magnetic coplanarity technique (e.g., B. Abraham-Shrauner & S. H. Yun 1976; C. T. Russell et al. 1983; A. F. Vinas & J. D. Scudder 1986; I. C. Jebaraj et al. 2024a) to find $\hat{\boldsymbol{n}}_{\rm sh}$ in RTN coordinates. For reference, the relevant upstream plasma and shock parameters[34] (see Appendix A for symbol definitions) are as follows:

1. *Plasma parameters*
   - $\langle B_o\rangle_{\rm up} \sim 531 \pm 6$ nT
   - $\langle V_{\rm bulk}\rangle_{\rm up} \sim 355 \pm 2$ km s^{-1}
   - $\langle n_e\rangle_{\rm up} \sim 2099 \pm 182$ cm^{-3}
   - $\langle T_{e,\rm tot}\rangle_{\rm up} \sim 92 \pm 7$ eV
   - $\langle T_{p,\rm tot}\rangle_{\rm up} \sim 36 \pm 3$ eV
   - $\langle f_{\rm ce}\rangle_{\rm up} \sim 14.9 \pm 0.17$ kHz
   - $\langle f_{\rm pe}\rangle_{\rm up} \sim 411 \pm 18$ kHz
   - $\langle \lambda_e\rangle_{\rm up} \sim 116 \pm 5$ m
   - $\langle \lambda_p\rangle_{\rm up} \sim 4.98 \pm 0.22$ km
   - $\langle \rho_{\rm ce}\rangle_{\rm up} \sim 61 \pm 2$ m
   - $\langle \rho_{\rm cp}\rangle_{\rm up} \sim 1.63 \pm 0.07$ km
   - $\langle \lambda_{\rm De}\rangle_{\rm up} \sim 1.55 \pm 0.09$ m
   - $\langle C_s\rangle_{\rm up} \sim 138 \pm 5$ km s^{-1}
   - $\langle V_{\rm A}\rangle_{\rm up} \sim 253 \pm 10$ km s^{-1}
   - $\langle V_{\rm ms}\rangle_{\rm up} \sim 288 \pm 11$ km s^{-1}
   - $\langle \beta_e\rangle_{\rm up} \sim 0.27 \pm 0.03$
   - $\langle \beta_p\rangle_{\rm up} \sim 0.11 \pm 0.01$
   - $\langle \beta_{\rm tot}\rangle_{\rm up} \sim 0.38 \pm 0.04$
2. *Shock parameters*
   - $\hat{\boldsymbol{n}}_{\rm sh}$ [RTN] $\sim$[+0.6545, +0.5829, −0.4814]
   - $\theta_{\rm Bn} \sim 50° \pm 2°$
   - $\langle V_f\rangle_{\rm up} \sim 277 \pm 12$ km s^{-1}
   - $\langle |V_{\rm shn}|\rangle_{\rm up} \sim 465 \pm 40$ km s^{-1}
   - $\langle |U_{\rm shn}|\rangle_{\rm up} \sim 334 \pm 30$ km s^{-1}
   - $\bar{R}_n \sim 1.96 \pm 0.24$
   - $\bar{R}_B \sim 1.98 \pm 0.03$
   - $\Delta\bar{B}_o \sim 589 \pm 146$ nT
   - $\langle M_{\rm A}\rangle_{\rm up} \sim 1.32 \pm 0.13$
   - $\langle M_{\rm Cs}\rangle_{\rm up} \sim 2.42 \pm 0.24$
   - $\langle M_{\rm ms}\rangle_{\rm up} \sim 1.16 \pm 0.11$
   - $\langle M_f\rangle_{\rm up} \sim 1.21 \pm 0.12$
   - $\left\langle \frac{M_f}{M_{\rm cr,1}} \right\rangle_{\rm up} \sim 0.5 \pm 0.06$
   - $\left\langle \frac{M_f}{M_{\rm ww}} \right\rangle_{\rm up} \sim 0.09 \pm 0.01$

We also examined the three so-called "mixed-mode methods" (e.g., B. Abraham-Shrauner & S. H. Yun 1976; C. T. Russell et al. 1983) for determining the shock normal and other shock parameters. All three yielded similar results to the magnetic coplanarity results shown above. In fact, the solutions for all three methods are remarkably stable with respect to each other. For instance, all three gave $\theta_{\rm Bn} \sim 52°$ and $\langle M_f\rangle_{\rm up} \sim 1.26$, which are within the range of uncertainties for all estimates. Thus, unless $\langle T_{e,\rm tot}\rangle_{\rm up}$ is wildly different from our statistical estimate above,[35] we are confident that this is a low Mach number, quasi-perpendicular shock.

[34] Note that prior statistical work found $T_{e,\rm tot} \sim 2.55 T_{p,\rm tot}$ following L. B. Wilson et al. (2023), which is used below for the electron temperatures since electron data is not currently available.

[35] Thermal effects can sometimes cause solutions to the full Rankine–Hugoniot relations to deviate from the solutions from magnetic coplanarity and the mixed-mode methods (e.g., A. F. Vinas & J. D. Scudder 1986; A. Szabo 1994; A. Koval & A. Szabo 2008).

Appendix C
Electric Field Calibration

In this appendix, we summarize how the electric field data were calibrated.

There have been several efforts to determine the effective antenna length, $L_{\rm eff}$, for the PSP FIELDS antenna (e.g., F. S. Mozer et al. 2020; S. Karbashewski et al. 2023; K.-E. Choi et al. 2024). It is particularly complicated because the plasma sheath gain appears to frequently exceed unity in the DC-coupled frequency range. This necessitates values for $L_{\rm eff}$ that are much greater than the physical separation of the antenna's electrical centers. The value of $L_{\rm eff}$ varies considerably with plasma conditions (e.g., density, temperature, etc.) and must be recalculated for each interval.

Further, the direction of the measured DC-coupled electric field measured by PSP appears to differ significantly from the direction given by the convective electric field. The differences most likely arise from the following factors: the antennas are not orthogonal, the antennas are short compared to the spacecraft, and there is a significant plasma wake caused by the spacecraft. For instance, we observe a significant wake effect in the T-component of the DC-coupled electric field (i.e., it differs significantly from that derived from the convective electric field).

The simplified process to correct the vector directions and amplitudes of the DC-coupled electric fields is as follows:

1 Calculate the convective electric field from the SPAN-I moments and the DC-coupled magnetic field measurements.
2 Determine the magnitude of $L_{\rm eff}$ necessary to get the measured DC-coupled electric field magnitude in the T–N plane to match that from the convective electric field.
3 Determine the angular rotation (in T–N plane) necessary to make the vector directions align between the measured DC-coupled electric field and convective electric field.

Note that interpolation, filtering, downsampling, etc., were all used during intermediate steps, but the above approach is the summarized methodology used.

Appendix D
MVA

In this appendix, we provide additional details regarding our use of MVA (e.g., A. V. Khrabrov & B. U. Ö. Sonnerup 1998).

The MVA details are described in previous work (e.g., L. B. Wilson et al. 2017; S. Giagkiozis et al. 2018), but the basic premise is that the data are broken up into frequency and temporal bins prior to performing MVA. Only the best, nonoverlapping MVA results are kept, where quality is defined by maximizing the intermediate-to-minimum, $\frac{\lambda_{\rm int}}{\lambda_{\rm min}}$, and minimizing the maximum-to-intermediate, $\frac{\lambda_{\rm max}}{\lambda_{\rm int}}$, eigenvalue ratios. For an interval to be kept, we require $\frac{\lambda_{\rm int}}{\lambda_{\rm min}} \geqslant 100$ and $\frac{\lambda_{\rm max}}{\lambda_{\rm int}} \leqslant 2$. For the whistler precursor observed between ∼07:50:27.500 UTC and ∼07:50:28.751 UTC, there were 181 unique MVA solutions, of which 102 satisfied the above eigenvalue ratio criteria.

Once we have the wave normal unit vectors, $\hat{\boldsymbol{k}}$, from MVA, we can calculate various wave normal angles, $\theta_{\rm kj}$. The three most relevant are those with respect to $\langle \boldsymbol{B}_o \rangle_{\rm up}$∼ $[-526,+9,-1]$ nT, $\langle \boldsymbol{V}_{\rm bulk} \rangle_{\rm up}$∼$[+318,-152,-22]$ km s^{-1}, and $\hat{\boldsymbol{n}}_{\rm sh}$∼$[+0.6545, +0.5829, -0.4814]$ (all in RTN coordinates). If we further define a latitude vector that is the cross-product between $\hat{\boldsymbol{n}}_{\rm sh}$ and $\langle \boldsymbol{B}_{\rm o} \rangle_{\rm up}$ to determine whether the wave propagates in or out of the plane containing both of these vectors, we define a fourth wave normal angle, $\theta_{k\lambda}$.[36]

With the $\hat{\boldsymbol{k}}$ and $\theta_{\rm kj}$ values from MVA, we can approximate the rest-frame parameters following the approach by L. B. Wilson et al. (2013) and L. B. Wilson et al. (2017). That is, we Doppler-shift the cold plasma whistler dispersion relation and invert to find the wavenumber, k, rest-frame frequency, ω, and rest-frame phase speed, $V_{\rm ph}$. As mentioned previously, the SPAN-I velocity moments are good in the upstream but have issues downstream of the shock ramp.[37] We use the $\langle \boldsymbol{V}_{\rm bulk} \rangle_{\rm up}$∼$[+318, -152, -22]$ km s^{-1} (RTN) for the transformation velocity. Since this is a cubic polynomial, every input will yield three roots. We found that one root was consistently unphysical because it had $\frac{\omega}{\Omega_{\rm ce}} \geqslant 0.95$ and $\frac{k}{\omega_{\rm pe}} c > 10$, i.e., PRF frequencies >10 kHz and wavelengths of a few meters. We thus ignored those solutions, which leaves us with four solutions for every root of the cubic equation: one each for $\pm\hat{\boldsymbol{k}}$ and one for the lower frequency bound and one for the upper frequency bound. Thus, every MVA solution has eight possible solutions from the cubic equation, i.e., two roots, two signs for $\hat{\boldsymbol{k}}$, and two spacecraft frame (SCF) frequencies.

Appendix E
Wave Amplitude Analysis

In this appendix, we provide additional details regarding our analysis of the PSP FIELDS data and the assumptions made.

The outer envelope is determined using a convex hull on a time window of the $\delta\boldsymbol{b}$, $\delta\boldsymbol{e}$, and $\delta\boldsymbol{s}$ data, then the time window is shifted, and the process is repeated. The time windows chosen were eight points wide, and the shift length was also eight points (i.e., 50% overlap). The envelope lines were then smoothed over seven points using a running boxcar average to reduce spikes. This resulted in 47 time stamps for $\delta\boldsymbol{b}$ and $\delta\boldsymbol{s}$ and 97 time stamps for $\delta\boldsymbol{e}$. From these envelopes, we could calculate the pk–pk wave amplitudes, $\delta b_{\rm pk-pk}$.

Note that we are interested in only the fluctuating components of the fields, which is why we perform a high-pass filter on the data above 1 Hz and then detrend that result using a 10 point boxcar averaging window. Strictly speaking, the electric field is frame dependent, but the relevant frames of reference at a shock involve static velocity transformations, the result would be a DC offset in one or more of the electric field components. This would be removed by both the high-pass filter and detrending performed on the data. We then define the Poynting flux as $\delta\boldsymbol{s}=(\delta\boldsymbol{e} \times \delta\boldsymbol{b})/2 \quad \mu_o$, where the factor of 2 comes from the fact that we only measure the real part of the fields.

PSP can only properly measure two components of the electric field, so we only get one component of the Poynting flux and partial values for the other two components. In the RTN coordinate basis, we measure the T- and N-components for $\delta\boldsymbol{e}$

[36] $\theta_{k\lambda}\sim 90^\circ$ would imply $\hat{\boldsymbol{k}}$ falls in the same plane as $\hat{\boldsymbol{n}}_{\rm sh}$ and $\langle \boldsymbol{B}_{\rm o} \rangle_{\rm up}$, i.e., coplanar.

[37] Thus, we rely upon the peak in the energy flux spectra to determine $\boldsymbol{V}_{\rm bulk}$ in both regions for consistency.

and thus get the full R-component for δs. The T- and N-components for δs are only partial values. The calibration of the electric fields is especially complicated as the effective antenna length can exceed the physical length of the antenna (e.g., see discussion in F. S. Mozer et al. 2020; S. Karbashewski et al. 2023; K.-E. Choi et al. 2024) (and see Appendix C).

Appendix F
Synchrotron Emission

In this appendix, we provide a very summarized discussion of the synchrotron emission analysis. More details can be found in I. C. Jebaraj et al. (2024b) and G. B. Rybicki & A. P. Lightman (1979).

In a recent study, I. C. Jebaraj et al. (2024b) demonstrated that transverse electromagnetic emissions observed above the upper hybrid frequency can be attributed to extraordinary mode radiation from relativistic electrons in strong magnetic fields. Synchrotron emission is an incoherent process in which individual electrons radiate as they spiral in a magnetic field. In our case, the observed emission likely originates from electrons accelerated into a power-law distribution by the shock. The location of the spectral peak in frequency provides an approximate estimate of the maximum energy at which the emission is suppressed by the background plasma (the so-called low-frequency turnover)—a suppression that may arise from various plasma processes (e.g., V. L. Ginzburg & S. I. Syrovatskii 1964; G. B. Rybicki & A. P. Lightman 1979).

The characteristic synchrotron emission frequency can be approximated by

$$f_{\rm sync} \sim \gamma^2 \quad f_{\rm ce}\,, \tag{F2}$$

where γ is the relativistic Lorentz factor and $f_{\rm ce}$ is the nonrelativistic electron cyclotron frequency (unsigned) defined in Appendix A.

We observe clear synchrotron emission between ~07:20:00 UTC and the shock ramp. The peak emission frequency during this interval is $f_{\rm sync}\sim$ 485–610 kHz, with a mean of ~534 kHz. The electron cyclotron frequency during the same time interval is $f_{\rm ce}\sim$ 13.87–15.63 kHz, with a mean of ~14.58 kHz. Solving Equation (F2) for γ gives ~5.6–6.6 or electron kinetic energies of ~2.3–2.8 MeV. This corresponds to electron speeds normalized to the vacuum speed of light of ~0.9838–0.9883. Note that there need not be a large fraction of emitting electrons. G. Mann et al. (2024) illustrated that the fraction of relativistic electrons to ambient may be as small as 10^{-3}–10^{-2} for similar Mach number shocks in the solar corona.

ORCID iDs

Lynn B. Wilson, III https://orcid.org/0000-0002-4313-1970
J. Grant Mitchell https://orcid.org/0000-0003-4501-5452
Adam Szabo https://orcid.org/0000-0003-3255-9071
Immanuel C. Jebaraj https://orcid.org/0000-0002-0606-7172
Michael L. Stevens https://orcid.org/0000-0002-7728-0085
David M. Malaspina https://orcid.org/0000-0003-1191-1558
Grant D. Berland https://orcid.org/0000-0001-6010-6374
Athanasios Kouloumvakos https://orcid.org/0000-0001-6589-4509
Stuart D. Bale https://orcid.org/0000-0002-1989-3596
Roberto Livi https://orcid.org/0000-0002-0396-0547
Jasper S. Halekas https://orcid.org/0000-0001-5258-6128
Christina M. S. Cohen https://orcid.org/0000-0002-0978-8127

References

Abraham-Shrauner, B., & Yun, S. H. 1976, JGR, 81, 2097
Anagnostopoulos, G. C., Sarris, E. T., & Krimigis, S. M. 1986, JGR, 91, 3020
Angelopoulos, V., Chapman, J. A., Mozer, F. S., et al. 2002, JGR, 107, 1181
Angelopoulos, V., Cruce, P., Drozdov, A., et al. 2019, SSRv, 215, 9
Bale, S. D., Goetz, K., Harvey, P. R., et al. 2016, SSRv, 204, 49
Balikhin, M. A., Alleyne, H. S.-C. K., Treumann, R. A., et al. 1999, JGR, 104, 12525
Blanco-Cano, X., Kajdič, P., Aguilar-Rodríguez, E., et al. 2016, JGRA, 121, 992
Caprioli, D., Pop, A.-R., & Spitkovsky, A. 2015, ApJL, 798, L28
Caprioli, D., & Spitkovsky, A. 2013, ApJL, 765, L20
Caprioli, D., & Spitkovsky, A. 2014a, ApJ, 783, 91
Caprioli, D., & Spitkovsky, A. 2014b, ApJ, 794, 47
Choi, K.-E., Agapitov, O., Colomban, L., et al. 2024, ApJ, 971, 177
Cohen, C. M. S., Leske, R. A., Christian, E. R., et al. 2024, ApJ, 966, 148
Coroniti, F. V. 1970, JPlPh, 4, 265
Courant, R., & Friedrichs, K. O. 1977, Supersonic Flow and Shock Waves (Berlin: Springer)
Decker, G., & Robson, A. E. 1972, PhRvL, 29, 1071
Dimmock, A. P., Balikhin, M. A., Walker, S. N., & Pope, S. A. 2013, AnGeo, 31, 1387
Dimmock, A. P., Khotyaintsev, Y. V., Lalti, A., et al. 2022, A&A, 660, A64
Do, T. M., Fraschetti, F., Kota, J., et al. 2025, ApJ, 979, 50
Edmiston, J. P., & Kennel, C. F. 1984, JPlPh, 32, 429
Fairfield, D. H. 1974, JGR, 79, 1368
Fairfield, D. H., & Feldman, W. C. 1975, JGR, 80, 515
Farris, M. H., Russell, C. T., & Thomsen, M. F. 1993, JGR, 98, 15285
Fox, N. J., Velli, M. C., Bale, S. D., et al. 2016, SSRv, 204, 7
Fränz, M., & Harper, D. 2002, P&SS, 50, 217
Galeev, A. A. 1976, in Proc. of the Intl. Symp. on Solar-Terrestrial Physics, Physics of Solar Planetary Environments, ed. D. J. Williams (Washington, DC: AGU), 464
Galeev, A. A., & Karpman, V. I. 1963, JETP, 17, 403, http://jetp.ras.ru/cgi-bin/e/index/e/17/2/p403?a=list
Giagkiozis, S., Wilson, L. B., III, Burch, J. L., et al. 2018, JGRA, 123, 5435
Ginzburg, V. L., & Syrovatskii, S. I. 1964, SvA, 8, 342
Greenstadt, E. W. 1985, in Collisionless Shocks in the Heliosphere: Reviews of Current Research, ed. B. T. Tsurutani & R. G. Stone, 35 (Washington, D. C: AGU), 169
Greenstadt, E. W., Scarf, F. L., Russell, C. T., Formisano, V., & Neugebauer, M. 1975, JGR, 80, 502
Greenstadt, E. W., Scarf, F. L., Russell, C. T., et al. 1977, JGR, 82, 651
Hill, M. E., Mitchell, D. G., Andrews, G. B., et al. 2017, JGRA, 122, 1513
Hobara, Y., Balikhin, M., Krasnoselskikh, V., Gedalin, M., & Yamagishi, H. 2010, JGRA, 115, 11106
Hull, A. J., Muschietti, L., Agapitov, O. V., et al. 2024, JGRA, 129, e2023JA031630
Hull, A. J., Muschietti, L., Le Contel, O., Dorelli, J. C., & Lindqvist, P. A. 2020, JGRA, 125, e27290
Hull, A. J., Muschietti, L., Oka, M., et al. 2012, JGRA, 117, 12104
Jebaraj, I. C., Agapitov, O., Krasnoselskikh, V., et al. 2024a, ApJL, 968, L8
Jebaraj, I. C., Agapitov, O. V., Gedalin, M., et al. 2024b, ApJL, 976, L7
Jebaraj, I. C., Dresing, N., Krasnoselskikh, V., et al. 2023, A&A, 680, L7
Kajdič, P., Blanco-Cano, X., Aguilar-Rodriguez, E., et al. 2012, JGRA, 117, 6103
Karbashewski, S., Agapitov, O. V., Kim, H. Y., et al. 2023, ApJ, 947, 73
Karpman, V. I. 1964, SPhD, 8, 919
Kasper, J. C., Abiad, R., Austin, G., et al. 2016, SSRv, 204, 131
Kennel, C. F. 1987, JGR, 92, 13427
Kennel, C. F., Edmiston, J. P., & Hada, T. 1985, in Collisionless Shocks in the Heliosphere: A Tutorial Review, ed. R. G. Stone & B. T. Tsurutani, Vol. 34 (Washington, D.C: AGU), 1
Khrabrov, A. V., & Sonnerup, B. U. Ö. 1998, JGR, 103, 6641
Kouloumvakos, A., Wijsen, N., Jebaraj, I. C., et al. 2025, ApJ, 979, 100
Koval, A., & Szabo, A. 2008, JGRA, 113, A10110
Krasnoselskikh, V. V., Lembège, B., Savoini, P., & Lobzin, V. V. 2002, PhPl, 9, 1192
Leroy, M. M., & Mangeney, A. 1984, AnGeo, 2, 449
Lin, R. P., Anderson, K. A., Ashford, S., et al. 1995, SSRv, 71, 125
Livi, R., Larson, D. E., Kasper, J. C., et al. 2022, ApJ, 938, 138
Malaspina, D. M., Ergun, R. E., Bolton, M., et al. 2016, JGRA, 121, 5088

Mann, G., Veronig, A. M., & Schuller, F. 2024, A&A, 686, A207
Mason, G. M., Gold, R. E., Krimigis, S. M., et al. 1998, SSRv, 86, 409
Mason, G. M., Korth, A., Walpole, P. H., et al. 2008, SSRv, 136, 257
Mazelle, C., Lembège, B., Morgenthaler, A., et al. 2010, in AIP Conf. Ser. Proc. 1216, 12th Intl. Solar Wind Conf. (Melville, NY: AIP), 471
McComas, D. J., Alexander, N., Angold, N., et al. 2016, SSRv, 204, 187
Mellott, M. M., & Greenstadt, E. W. 1984, JGR, 89, 2151
Mitchell, J. G., Christian, E. R., de Nolfo, G. A., et al. 2025, ApJ, 980, 96
Mitchell, J. G., De Nolfo, G. A., Hill, M. E., et al. 2021, ApJ, 919, 119
Morton, K. W. 1964, PhFl, 7, 1800
Mozer, F. S., Agapitov, O. V., Bale, S. D., et al. 2020, JGRA, 125, e27980
Newbury, J. A., & Russell, C. T. 1996, GeoRL, 23, 781
Newbury, J. A., Russell, C. T., & Gedalin, M. 1998, JGR, 1032, 29581
Oka, M., Otsuka, F., Matsukiyo, S., et al. 2019, ApJ, 886, 53
Ramírez Vélez, J. C., Blanco-Cano, X., Aguilar-Rodriguez, E., et al. 2012, JGRA, 117, A11103
Raptis, S., Lalti, A., Lindberg, M., et al. 2025, NatCo, 16, 488
Russell, C. T. 1988, AdSpR, 8, 147
Russell, C. T., Gosling, J. T., Zwickl, R. D., & Smith, E. J. 1983, JGR, 88, 9941
Rybicki, G. B., & Lightman, A. P. 1979, Radiative Processes in Astrophysics (New York: Wiley)
Sagdeev, R. Z. 1966, RvPP, 4, 23
Sarris, E. T., Anagnostopoulos, G. C., & Krimigis, S. M. 1987, JGR, 92, 12083
Shi, X., Artemyev, A., Angelopoulos, V., Liu, T. Z., & Wilson III, L. B. 2025, NatCo, 16, 11
Shu, F. H. 1992, Physics of Astrophysics, Vol. II (Melville, NY: Univ. Science Books),
Stansby, D., Horbury, T. S., Chen, C. H. K., & Matteini, L. 2016, ApJL, 829, L16
Stepanov, A., Zaitsev, V., & Valtaoja, E. 2011, BaltA, 20, 275
Stepanov, A. V., & Zaitsev, V. V. 2013, in IAU Symp. 291, Neutron Stars and Pulsars: Challenges and Opportunities after 80 years, ed. J. van Leeuwen (Cambridge: Cambridge Univ. Press), 505
Stringer, T. E. 1963, JNuE, 5, 89
Sundkvist, D., Krasnoselskikh, V., Bale, S. D., et al. 2012, PhRvL, 108, 025002
Szabo, A. 1994, JGR, 99, 14737
Tidman, D. A., & Krall, N. A. 1971, Shock Waves in Collisionless Plasmas (New York: John Wiley & Sons, Inc.),
Tidman, D. A., & Northrop, T. G. 1968, JGR, 73, 1543
Treumann, R. A. 2009, A&ARv, 17, 409
Vinas, A. F., & Scudder, J. D. 1986, JGR, 91, 39
Walker, S. N., Balikhin, M. A., & Nozdrachev, M. N. 1999, GeoRL, 26, 1357
Wiedenbeck, M. E., Angold, N. G., Birdwell, B., et al. 2017, ICRC (Busan, Korea), 301, 16
Wilson, L. B., III 2016, in Low-frequency Waves in Space Plasmas, ed. A. Keiling, D.-H. Lee, & V. Nakariakov, 216 (Washington, DC: AGU), 269
Wilson, L. B., III 2022, lynnbwilsoniii/wind_3dp_pros: Space Plasma Missions IDL Software Library v1.0.2, Zenodo,
Wilson, L. B., III, Brosius, A. L., Gopalswamy, N., et al. 2021a, RvGeo, 59, e2020RG000714
Wilson, L. B., III, Cattell, C. A., Kellogg, P. J., et al. 2009, JGRA, 114, 10106
Wilson, L. B., III, Chen, L.-J., & Roytershteyn, V. 2021b, FrASS, 7, 97
Wilson, L. B., III, Koval, A., Szabo, A., et al. 2012, GeoRL, 39, 8109
Wilson, L. B., III, Koval, A., Szabo, A., et al. 2013, JGRA, 118, 5
Wilson, L. B., III, Koval, A., Szabo, A., et al. 2017, JGRA, 122, 9115
Wilson, L. B., III, Sibeck, D. G., Breneman, A. W., et al. 2014a, JGRA, 119, 6455
Wilson, L. B., III, Sibeck, D. G., Breneman, A. W., et al. 2014b, JGRA, 119, 6475
Wilson, L. B., III, Sibeck, D. G., Turner, D. L., et al. 2016, PhRvL, 117, 215101
Wilson, L. B., III, Stevens, M. L., Kasper, J. C., et al. 2018, ApJS, 236, 41
Wilson, L. B., III, Stevens, M. L., Kasper, J. C., et al. 2023, ApJS, 269, 62
Wu, C. S. 1984, JGR, 89, 8857
Wygant, J. R., Keiling, A., Cattell, C. A., et al. 2000, JGR, 105, 18675